

## Solar-to-fuels conversion over In<sub>2</sub>O<sub>3</sub>/g-C<sub>3</sub>N<sub>4</sub> hybrid photocatalysts

Liao, Yusen; Cao, Shao-Wen; Liu, Xin-Feng; Yuan, Yu-Peng; Zhang, Zhenyi; Fang, Jun; Loo, Say Chye Joachim; Sum, Tze Chien; Xue, Can

2013

Cao, S. W., Liu, X. F., Yuan, Y. P., Zhang, Z., Liao, Y. S., Fang, J., et al. (2014). Solar-to-fuels conversion over In<sub>2</sub>O<sub>3</sub>/g-C<sub>3</sub>N<sub>4</sub> hybrid photocatalysts. *Applied catalysis B: Environmental*, 147, 940–946.

<https://hdl.handle.net/10356/100079>

<https://doi.org/10.1016/j.apcatb.2013.10.029>

---

© 2013 Elsevier B.V. This is the author created version of a work that has been peer reviewed and accepted for publication by *Applied Catalysis B: Environmental*, Elsevier B.V. It incorporates referee's comments but changes resulting from the publishing process, such as copyediting, structural formatting, may not be reflected in this document. The published version is available at: [<http://dx.doi.org/10.1016/j.apcatb.2013.10.029>].

*Downloaded on 25 Aug 2022 02:19:48 SGT*

# Solar-to-Fuels Conversion over $\text{In}_2\text{O}_3/\text{g-C}_3\text{N}_4$ Hybrid Photocatalysts

Shao-Wen Cao <sup>a</sup>, Xin-Feng Liu <sup>b</sup>, Yu-Peng Yuan <sup>a,c</sup>, Zhen-Yi Zhang <sup>a</sup>, Yu-Sen Liao <sup>a</sup>,  
Jun Fang <sup>a</sup>, Say Chye Joachim Loo <sup>a,\*</sup>, Tze Chien Sum <sup>b</sup>, Can Xue <sup>a,\*</sup>

<sup>a</sup>*Solar Fuels Lab, School of Materials Science and Engineering, Nanyang Technological University, Singapore 639798 (Singapore)*

<sup>b</sup>*Division of Physics and Applied Physics, School of Physical of Mathematical Sciences, Nanyang Technological University, Singapore 637371 (Singapore)*

<sup>c</sup>*Laboratory of Advanced Porous Materials, School of Chemistry and Chemical Engineering, Anhui University, Hefei, 230039, P.R.China*

\* Corresponding author:

Tel: +65-67906180; Fax:+65-67909081;

E-mail: cxue@ntu.edu.sg; joachimloo@ntu.edu.sg

## **Abstract**

We have achieved in-situ growth of  $\text{In}_2\text{O}_3$  nanocrystals onto the sheet-like  $\text{g-C}_3\text{N}_4$  surface. The resulting  $\text{In}_2\text{O}_3$ - $\text{g-C}_3\text{N}_4$  hybrid structures exhibit considerable improvement on the photocatalytic activities for  $\text{H}_2$  generation and  $\text{CO}_2$  reduction. The enhanced activities are attributed to the interfacial transfer of photogenerated electrons and holes between  $\text{g-C}_3\text{N}_4$  and  $\text{In}_2\text{O}_3$ , leading to effective charge separation on both parts. Further studies by transient PL spectroscopy confirm that the  $\text{In}_2\text{O}_3$ - $\text{g-C}_3\text{N}_4$  heterojunctions remarkably promote the charge transfer efficiency, thereby increase the charge carrier lifetime for the photocatalytic reactions.

**Keywords:** Photocatalysis; hydrogen production;  $\text{CO}_2$  reduction; graphitic carbon nitride; Charge transfer.

## 1. Introduction

The fuels production through solar-driven water splitting or CO<sub>2</sub> reduction has been considered as a promising way to solve the worldwide energy shortage [1-3]. In the past decade, great efforts have been made to explore solar-to-fuel conversion by using various semiconductor photocatalysts including TiO<sub>2</sub> [4,5], Cu<sub>2</sub>O [6,7], SrTiO<sub>3</sub> [8,9], ZnFe<sub>2</sub>O<sub>4</sub> [10], CdS [11,12], InVO<sub>4</sub> [13] etc. Among them, In<sub>2</sub>O<sub>3</sub> is known as a semiconductor with an indirect bandgap of ~2.8 eV, and has been proved as a visible-light-active photocatalyst [14,15], and has also been used as the efficient sensitizer to extend the absorption spectra of oxide semiconductor photocatalysts from the UV region into visible region [16-18]. More recently, a new type of polymeric nanosheet structure, graphitic carbon nitride (g-C<sub>3</sub>N<sub>4</sub>), has been introduced as a visible-light photocatalyst for water splitting due to its unique electronic band structure with high thermal and chemical stability [19-21].

In the development of semiconductor-based photocatalysts for solar-to-fuel conversion, one disconcerting drawback is the high recombination rate of photogenerated electron-hole pairs in the individual semiconductor structure [22]. Thus it is very critical to modulate the charge carrier dynamics in semiconductor structures. One effective way is coupling two semiconductor units with appropriate band alignment between the two units to allow interfacial charge transfer upon excitation and promote the separation efficiency of photogenerated electrons and holes [23-29]. Thus the charge carrier lifetime can be significantly improved to enable desired surface reactions and thereby enhance the photocatalytic efficiency for

solar-to-fuels conversion.

Recently researchers have found that two-dimensional (2-D) semiconductor nanostructures offer higher charge mobility and lower recombination rates of charge carriers as compared to 0-D spherical nanoparticles [30,31]. Herein, we present a prototype of 0D-2D semiconductor heterojunction system by in-situ growth of  $\text{In}_2\text{O}_3$  nanocrystals on g- $\text{C}_3\text{N}_4$  nanosheets through a simple solvothermal method. The well-dispersed  $\text{In}_2\text{O}_3$  nanocrystals on sheet-like g- $\text{C}_3\text{N}_4$  surfaces form intimate contact, which allows for effective interfacial charge transfer across the  $\text{In}_2\text{O}_3/\text{g-C}_3\text{N}_4$  heterojunction since the conduction band (CB) and valance band (VB) positions of  $\text{In}_2\text{O}_3$  ( $\sim -0.6$  eV and  $\sim +2.2$  eV, respectively, vs. NHE) [28,29] are both lower than those of g- $\text{C}_3\text{N}_4$  ( $\sim -1.1$  eV and  $\sim +1.6$  eV, respectively, vs. NHE) [19,32]. In particular, the conduction band edge ( $\sim -0.6$  eV) of  $\text{In}_2\text{O}_3$  is high enough for reduction of proton and  $\text{CO}_2$ . As such, we found that the  $\text{In}_2\text{O}_3/\text{g-C}_3\text{N}_4$  hybrid structures are capable for efficient photocatalytic  $\text{H}_2$  generation and  $\text{CO}_2$  reduction with much higher activities than the pure  $\text{In}_2\text{O}_3$  and g- $\text{C}_3\text{N}_4$ . This is attributed to the highly effective charge separation on  $\text{In}_2\text{O}_3/\text{g-C}_3\text{N}_4$  hybrids as confirmed by the transient photoluminescence (PL) spectroscopy.

## 2. Experiments

### 2.1 Preparation of $\text{In}_2\text{O}_3$ -g- $\text{C}_3\text{N}_4$ hybrids

g- $\text{C}_3\text{N}_4$  powder was synthesized by heating 6 g melamine in an alumina crucible with a cover at 500 °C in a muffle furnace for 2 h at a heating rate of 20 °C /min, and

further heated to 520 °C for another 2 h at a heating rate of 5 °C/min [33]. In-situ growth of In<sub>2</sub>O<sub>3</sub> nanocrystals (10 wt%) on g-C<sub>3</sub>N<sub>4</sub> nanosheets was carried out as following steps. While stirring, 0.5 mmol of In(Ac)<sub>3</sub> and 600 mg of the as-prepared g-C<sub>3</sub>N<sub>4</sub> were added into 50 mL dimethyl sulfoxide (DMSO). The resultant suspension was sealed in a 100 mL teflon-lined stainless-steel autoclave. The autoclave was heated to 180 °C and maintained for 12 h, and then allowed to cool to room temperature. The product was collected after centrifugation, washed with water and ethanol repeatedly, and then dried in a vacuum oven. Pure In<sub>2</sub>O<sub>3</sub> and other In<sub>2</sub>O<sub>3</sub>-g-C<sub>3</sub>N<sub>4</sub> hybrids with different ratio were synthesized using the similar route by tuning the dosage of g-C<sub>3</sub>N<sub>4</sub>.

## 2.2 Characterization

A Shimadzu XRD-6000 X-ray diffractometer (Cu K $\alpha$  source) was used to record X-ray powder diffraction (XRD) patterns with the 2 $\theta$  range from 5 to 80° at a scan rate of 1 °/min. Transmission electron microscopy (TEM) images were obtained from a JEOL JEM-2100F transmission electron microscope at an accelerating voltage of 200 kV. UV–vis diffuse reflectance spectra (DRS) were taken with a Lambda 750 UV/Vis/NIR spectrophotometer (Perkin Elmer, USA). X-ray Photoelectron spectroscopy (XPS) measurement was performed on a Thermo Scientific Theta Probe XPS with monochromatized Al K $\alpha$  ( $h\nu=1486.6$  eV) source. The steady-state photoluminescence (PL) spectra were obtained by a Shimadzu RF-5310PC fluorometer at an excitation wavelength of 325 nm.

## 2.3 Transient optical spectroscopy

For time-resolved PL measurements, the excitation pulse (325 nm) was generated from an optical parametric amplifier (TOPASTM, Light Conversion Ltd). The time-resolved PL spectra were obtained using a streak camera (Optronics GmbH) with a time resolution of 10 ps. The PL decay profile is fitted by using multiexponential function [34,35].

$$I_t = \sum_{i=1}^n A_i \exp\left(-\frac{t}{\tau_i}\right)$$

where  $I_t$  is intensity,  $A_i$  is the relative magnitude of the  $i$ th decay and  $\tau_i$  is the  $i$ th decay time.

#### *2.4 Photocatalytic hydrogen evolution*

Typically, 5 mg of the prepared photocatalysts were suspended in 10 mL aqueous solution of 0.1 M L-ascorbic acid (pH=4.0). Pt cocatalyst (0.5 wt%) was in-situ loaded by adding 61  $\mu$ L of  $H_2PtCl_6$  (0.08 wt%) aqueous solution into the suspension followed by the irradiation of a 300-W xenon lamp (MAX-302, Asahi Spectra, USA) coupled with a UV cut-off filter ( $\lambda > 420$  nm). The suspension was then purged with argon to drive away the residual air before sealed in a quartz flask. The photocatalytic hydrogen evolution was carried out by irradiating the suspension with a 300-W xenon lamp (MAX-302, Asahi Spectra, USA) coupled with a UV cut-off filter ( $\lambda > 420$  nm). The output light intensity is 200 mW/cm<sup>2</sup>. The gas product composition was analyzed periodically by an Agilent 7890A gas chromatograph (GC) with TCD detector.

#### *2.5 Photocatalytic CO<sub>2</sub> reduction*

In the photocatalytic reduction of CO<sub>2</sub>, 20 mg of the sample was uniformly

dispersed on a glass substrate with a base area of  $2.5 \times 2.5 \text{ cm}^2$ , which was then put into a quartz reactor (90 mL). Prior to irradiation, the reactor was purged with high-purity  $\text{CO}_2$  gas and 0.1 mL ultrapure water was injected into the reactor. A 500-W Xenon lamp (Newport, USA) with output light intensity of  $1200 \text{ mW/cm}^2$  was used as the light source for the photocatalytic reaction. During the irradiation, the gas product was taken from the reaction cell at given intervals to quantitatively analyze gas product composition by an Agilent 7890A gas chromatograph (GC) with TCD detector.

### *2.6 Photoelectrochemical measurements*

Photocurrent measurements were performed on an electrochemical workstation (CHI852c, CH Instruments) with a three-electrode configuration. Our sample, Ag/AgCl electrode, and Pt-wire electrode were employed as the working, reference, and counter electrode, respectively. Irradiation was carried out by using a 300-W xenon lamp (MAX-302, Asahi Spectra, USA) coupled with a UV cut-off filter ( $\lambda > 420 \text{ nm}$ ) and an output intensity of  $200 \text{ mW/cm}^2$ . The  $\text{Na}_2\text{SO}_4$  solution (0.1 M) was used as the electrolyte. The working electrodes were prepared by spreading aqueous slurries of various samples on FTO glass substrate, using adhesive tapes as spaces to obtain a  $1 \text{ cm} \times 1 \text{ cm}$  electrode. The applied bias was set as 0.4 V.

## **3. Results and discussion**

The XRD patterns of the as-prepared  $\text{g-C}_3\text{N}_4$ ,  $\text{In}_2\text{O}_3$ , and  $\text{In}_2\text{O}_3\text{-C}_3\text{N}_4$  hybrids (10 wt%  $\text{In}_2\text{O}_3$ ) are shown in Fig. 1. Two pronounced diffraction peaks locate at  $27.4^\circ$



and  $13.1^\circ$  for  $\text{g-C}_3\text{N}_4$ , which could be ascribed to the characteristic interlayer stacking peak of aromatic systems as the (002) peak for graphitic materials, and the interplanar separation as the (100) peak, respectively [33,36]. The XRD pattern of  $\text{In}_2\text{O}_3$  gives rise to six distinct diffraction peaks at  $21.5^\circ$ ,  $30.6^\circ$ ,  $35.6^\circ$ ,  $45.4^\circ$ ,  $50.9^\circ$ , and  $60.8^\circ$ , which can be attributed to the (211), (222), (400), (431), (440), and (622) crystal planes of cubic  $\text{In}_2\text{O}_3$  (JCPDS No. 71-2194), respectively. The  $\text{In}_2\text{O}_3$ - $\text{g-C}_3\text{N}_4$  hybrids exhibit characteristic XRD peaks of both  $\text{In}_2\text{O}_3$  and  $\text{g-C}_3\text{N}_4$ .

TEM and SEM images (Fig. 2) are taken to directly analyze the structures of the samples. Fig. 2a indicates that the polymeric  $\text{g-C}_3\text{N}_4$  has a sheet-like structure. The pure  $\text{In}_2\text{O}_3$  sample prepared without  $\text{g-C}_3\text{N}_4$  is shown as nanoparticle aggregation (Fig. 2b). However, in the presence of  $\text{g-C}_3\text{N}_4$ , the solvothermal process generated small  $\text{In}_2\text{O}_3$  nanocrystals well spreading on the  $\text{g-C}_3\text{N}_4$  surface, as shown by Fig. 2c. The HRTEM image (Fig. 2d) confirms the existence of small  $\text{In}_2\text{O}_3$  nanocrystals, and the lattice fringes with d spacing of 0.293 nm can be assigned to the (222) crystal plane of cubic  $\text{In}_2\text{O}_3$ .

Fig. 3 shows the absorption spectra of the prepared  $\text{g-C}_3\text{N}_4$ ,  $\text{In}_2\text{O}_3$ , and  $\text{In}_2\text{O}_3$ - $\text{g-C}_3\text{N}_4$  hybrid (10 wt%  $\text{In}_2\text{O}_3$ ). The pure  $\text{g-C}_3\text{N}_4$  and  $\text{In}_2\text{O}_3$  samples presented a similar absorption edge at  $\sim 450$  nm with wide overlap between their absorption spectra, thereby the absorption feature of the  $\text{In}_2\text{O}_3$ - $\text{g-C}_3\text{N}_4$  hybrids showed very little difference with that of pure  $\text{g-C}_3\text{N}_4$ . We further examine the  $\text{In}_2\text{O}_3$ - $\text{g-C}_3\text{N}_4$  hybrid (10 wt%  $\text{In}_2\text{O}_3$ ) through XPS. As shown in Fig. 4a, the peak of C 1s binding energies at 284.6 eV and 288.2 eV can be ascribed to  $\text{sp}^2$  C-C bonds and

sp<sup>2</sup>-bonded carbon in N-containing aromatic rings (N–C=N), respectively, which are the major carbon species in the g-C<sub>3</sub>N<sub>4</sub> [37,38]. The weak shoulder that can be deconvoluted into a peak at 285.8 eV could be assigned to sp<sup>3</sup>-coordinated carbon bonds from the defects on g-C<sub>3</sub>N<sub>4</sub> surface [21,36]. The N 1s spectrum showed two clear peaks (Fig. 4b) at 398.7 eV and 401.1 eV, corresponding to sp<sup>2</sup>-bonded N involved in the triazine rings (C–N=C) and amino groups (C–N–H). And the tiny shoulder between these two peaks can be deconvoluted into a peak at 399.8 eV caused by the tertiary nitrogen N–(C)<sub>3</sub> groups [39,40]. The binding energies of In 3d locate at 444.4 and 451.9 eV (Fig. 4c), which can be assigned to the In<sup>3+</sup> in In<sub>2</sub>O<sub>3</sub> nanocrystals [29,41]. The O 1s peaks at 529.7 and 531.5 eV (Fig. 4d) can be assigned to the oxygen in In<sub>2</sub>O<sub>3</sub> nanocrystals.

Photocatalytic activities of the prepared samples for hydrogen evolution under visible light ( $\lambda > 420$  nm) irradiation were evaluated by using L-ascorbic acid as the sacrificial reagent to consume photoinduced holes, and 0.5 wt% Pt was in-situ deposited as cocatalyst onto the samples to reduce the overpotential of H<sub>2</sub> evolution. L-ascorbic acid has been proved as an effective water soluble electron donor since its ascorbate anion can function as reductive quencher and also allows for the incorporation of a large amount of L-ascorbic acid in the aqueous reaction system [42-44]. Fig. 5a shows the H<sub>2</sub> evolution plots by g-C<sub>3</sub>N<sub>4</sub>, In<sub>2</sub>O<sub>3</sub>, and In<sub>2</sub>O<sub>3</sub>-g-C<sub>3</sub>N<sub>4</sub> hybrids (10 wt% In<sub>2</sub>O<sub>3</sub>) as a function of irradiation time. The pure In<sub>2</sub>O<sub>3</sub> sample did not show noticeable H<sub>2</sub> evolution, and the pure g-C<sub>3</sub>N<sub>4</sub> showed a H<sub>2</sub> generation rate of 0.19  $\mu\text{mol/h}$ . Remarkably, when 10 wt% In<sub>2</sub>O<sub>3</sub> nanocrystals are decorated on

g-C<sub>3</sub>N<sub>4</sub> surfaces, the hybrid structure exhibited 5 times higher H<sub>2</sub> generation rate (0.99 umol/h) than the pure g-C<sub>3</sub>N<sub>4</sub>.

However, the decoration content of In<sub>2</sub>O<sub>3</sub> showed considerable influence on the photocatalytic activity of the In<sub>2</sub>O<sub>3</sub>-g-C<sub>3</sub>N<sub>4</sub> hybrids. Even with small amount of In<sub>2</sub>O<sub>3</sub> (2.5 wt%) nanocrystals on g-C<sub>3</sub>N<sub>4</sub> surfaces, the H<sub>2</sub> evolution amount can be 2.4 times higher than that of pure g-C<sub>3</sub>N<sub>4</sub>. As shown in Fig. 5b, the photocatalytic activity of the In<sub>2</sub>O<sub>3</sub>-g-C<sub>3</sub>N<sub>4</sub> hybrids increases with more H<sub>2</sub> generation as the In<sub>2</sub>O<sub>3</sub> content rise to 10 wt%. However, excessive In<sub>2</sub>O<sub>3</sub> nanocrystals (>10 wt%) grown on g-C<sub>3</sub>N<sub>4</sub> surfaces led to decreased photocatalytic activity in H<sub>2</sub> generation, which might be due to the aggregation of In<sub>2</sub>O<sub>3</sub> nanocrystals. As shown in Fig. 6a, in the hybrid sample with 20 wt% In<sub>2</sub>O<sub>3</sub>, excess In<sub>2</sub>O<sub>3</sub> nanocrystals are aggregating on the g-C<sub>3</sub>N<sub>4</sub> surface, which reduces the interface area between In<sub>2</sub>O<sub>3</sub> and g-C<sub>3</sub>N<sub>4</sub> and thereby lower the charge separation efficiency relying on interfacial electron transfer. In addition, over-coverage of In<sub>2</sub>O<sub>3</sub> may reduce reactive sites on g-C<sub>3</sub>N<sub>4</sub> surfaces that are needed to quench the holes. This would also cause decreased photocatalytic activity. In short, our observation indicates that the optimal decoration amount of In<sub>2</sub>O<sub>3</sub> nanocrystals is 10 wt% to obtain the highest photocatalytic activity for H<sub>2</sub> generation. We further explore the stability of the optimal In<sub>2</sub>O<sub>3</sub>-g-C<sub>3</sub>N<sub>4</sub> hybrids (10 wt% In<sub>2</sub>O<sub>3</sub>) by a four-run cycling test of photocatalytic hydrogen evolution. Fig. 6b reveals that no obvious decrease of H<sub>2</sub> evolution was observed after the four cycles under 16-h visible light irradiation, suggesting the excellent stability of the In<sub>2</sub>O<sub>3</sub>-g-C<sub>3</sub>N<sub>4</sub> hybrids in the reactions.

In order to further demonstrate the improved photocatalytic activity by the in-situ grown  $\text{In}_2\text{O}_3$  nanocrystals on  $\text{g-C}_3\text{N}_4$ , the prepared samples were evaluated by using reaction of photocatalytic  $\text{CO}_2$  reduction into hydrocarbon fuels that is known as a challenging but promising application for sustainable energy resources [45-47]. As shown in Fig. 7a, after 4-h irradiation, the optimal  $\text{In}_2\text{O}_3$ - $\text{g-C}_3\text{N}_4$  hybrids with 10 wt%  $\text{In}_2\text{O}_3$  exhibited a  $\text{CH}_4$  production yield of 76.7 ppm (over 20 mg samples) without any cocatalyst, which is more than 3 times higher than that of pure  $\text{g-C}_3\text{N}_4$  and more than 4 times higher than that of pure  $\text{In}_2\text{O}_3$ . The influence of  $\text{In}_2\text{O}_3$  loading content on the  $\text{CH}_4$  production yield showed a similar trend with that on photocatalytic  $\text{H}_2$  generation. Note that these tests of photocatalytic  $\text{CO}_2$  reduction were carried out without loading any cocatalyst. Indeed, if we photo-deposited 0.5 wt% Pt-cocatalyst onto the  $\text{In}_2\text{O}_3$ - $\text{g-C}_3\text{N}_4$  hybrids (10 wt%  $\text{In}_2\text{O}_3$ ), the  $\text{CH}_4$  production yield could be further promoted to 159.2 ppm upon 4-h irradiation. This indicates that in the photocatalytic  $\text{CO}_2$  reduction, the Pt cocatalyst still can act as electron sinks to effectively improve the charge separation of the  $\text{In}_2\text{O}_3$ - $\text{g-C}_3\text{N}_4$  hybrid structure.

We also carried out the photoelectrochemical measurements to obtain the transient photocurrent responses for the samples of  $\text{g-C}_3\text{N}_4$ ,  $\text{In}_2\text{O}_3$ , and 10 wt%  $\text{In}_2\text{O}_3$ - $\text{g-C}_3\text{N}_4$  under several on-off cycles of irradiation. As shown in Fig. 8, The  $\text{In}_2\text{O}_3$ - $\text{g-C}_3\text{N}_4$  hybrid sample shows the highest photocurrent intensity among the three samples. This observation indicates that the formed  $\text{In}_2\text{O}_3$ - $\text{g-C}_3\text{N}_4$  heterojunctions allow for the more efficient separation of photogenerated

electron-hole pairs as compared to the individual g-C<sub>3</sub>N<sub>4</sub> and In<sub>2</sub>O<sub>3</sub>.

On the basis of the above experimental results, we believe that the enhanced photocatalytic activities by the in-situ grown In<sub>2</sub>O<sub>3</sub> nanocrystals are attributed to the interfacial transfer of photogenerated electrons and holes between g-C<sub>3</sub>N<sub>4</sub> and In<sub>2</sub>O<sub>3</sub>, which leads to effective charge separation on both parts. To further prove this assumption, we performed measurements by using both steady-state and transient photoluminescence (PL) spectroscopy. Fig. 9a shows that at an excitation wavelength of 325 nm, the pure g-C<sub>3</sub>N<sub>4</sub> sample exhibits a strong emission peak centered at ~450 nm. In comparison, when 10 wt% In<sub>2</sub>O<sub>3</sub> nanocrystals were present on the g-C<sub>3</sub>N<sub>4</sub> surface, the intensity of this emission band dropped significantly, indicating efficient transfer of photoexcited electrons from g-C<sub>3</sub>N<sub>4</sub> to In<sub>2</sub>O<sub>3</sub> nanocrystals. The lifetime of charge carriers in the In<sub>2</sub>O<sub>3</sub>-g-C<sub>3</sub>N<sub>4</sub> hybrids (10 wt% In<sub>2</sub>O<sub>3</sub>) were examined by using time-resolved transient PL spectroscopy, as shown in Fig. 9b. The fitted lifetimes of the PL decay profile are listed in Table 1. The pure g-C<sub>3</sub>N<sub>4</sub> sample exhibits only one radiative lifetime of 3 ns, which is associated with the photoexcited electron-hole pairs in g-C<sub>3</sub>N<sub>4</sub> that eventually undergo recombination [48]. While for the In<sub>2</sub>O<sub>3</sub>-g-C<sub>3</sub>N<sub>4</sub> hybrids, a shorter PL lifetime component ( $\tau_1=0.71$  ns with a weighing factor  $A_1 = 54.7\%$ ) appears, suggesting that some excited electrons undergo rapid transfer from g-C<sub>3</sub>N<sub>4</sub> to In<sub>2</sub>O<sub>3</sub>. This evidence of fast electron-injection confirms that the formation of In<sub>2</sub>O<sub>3</sub>-g-C<sub>3</sub>N<sub>4</sub> heterostructures remarkably promotes charge transfer efficiency, thereby favoring the photocatalytic reactions for H<sub>2</sub> evolution and CO<sub>2</sub> reduction.

Fig. 10 shows the schematic illustration of the possible photocatalytic mechanism. The enhanced photocatalytic activity could be attributed to the effective interfacial charge transfer between  $\text{In}_2\text{O}_3$  and  $\text{g-C}_3\text{N}_4$  across the heterojunction. Since the CB of  $\text{g-C}_3\text{N}_4$  ( $\sim -1.1$  eV vs. NHE) is more negative than that of  $\text{In}_2\text{O}_3$  ( $\sim -0.6$  eV vs. NHE), the photoexcited electrons on the CB of  $\text{g-C}_3\text{N}_4$  can rapidly transfer to the CB of  $\text{In}_2\text{O}_3$ . These accumulated electrons, together with the electrons excited from the VB of  $\text{In}_2\text{O}_3$ , are capable of reducing  $\text{H}^+$  and/or  $\text{CO}_2$  into valuable fuels. While the corresponding VB position of  $\text{In}_2\text{O}_3$  ( $\sim +2.2$  eV vs. NHE) is more positive than that of  $\text{g-C}_3\text{N}_4$  ( $\sim +1.6$  eV vs. NHE), the photogenerated holes on the VB of  $\text{In}_2\text{O}_3$  can migrate to the VB of  $\text{g-C}_3\text{N}_4$ , subsequently to oxidize the electron donor (ascorbic acid for  $\text{H}_2$  production and  $\text{OH}^-$  for  $\text{CO}_2$  reduction, respectively). As such, effective charge separation can be achieved, resulting in longer lifetime of the photogenerated charge carriers and thereby enhanced photocatalytic activities.

#### 4. Conclusions

In summary, we have successfully prepared  $\text{In}_2\text{O}_3/\text{g-C}_3\text{N}_4$  hybrid structures through a simple solvothermal method. A small amount of  $\text{In}_2\text{O}_3$  nanocrystals grown onto  $\text{g-C}_3\text{N}_4$  surfaces leads to considerable improvement on the photocatalytic activities for  $\text{H}_2$  evolution and  $\text{CO}_2$  reduction. The enhanced activities are attributed to the effective interfacial charge transfer across the  $\text{In}_2\text{O}_3/\text{g-C}_3\text{N}_4$  heterojunction, as evidenced by steady-state and transient PL studies. This work provides a new insight on developing 0D-2D semiconductor hetero-structured systems with effective charge

separation for highly efficient solar-to-fuels conversion.

## **Acknowledgements**

This work is financially supported by NTU seed funding for Solar Fuels Laboratory, MOE AcRF-Tier1 RG 44/11, MOE AcRF-Tier2 (MOE2012-T2-2-041, ARC 5/13), and CRP program (NRF-CRP5-2009-04) from the Singapore National Research Foundation (NRF). Y. P. Yuan acknowledges the support from the National Natural Science Foundation of China (No. 51002001).

## **References**

- [1] H. Tong, S.X. Ouyang, Y.P. Bi, N. Umezawa, M. Oshikiri, J.H. Ye, *Advanced Materials* 24 (2012) 229-251.
- [2] A. Kudo, Y. Miseki, *Chemical Society Reviews* 38 (2009) 253-278.
- [3] L. Ge, C.C. Han, *Applied Catalysis B: Environmental* 117-118 (2012) 268-274.
- [4] Z.Y. Yin, Z. Wang, Y.P. Du, X.Y. Qi, Y.Z. Huang, C. Xue, H. Zhang, *Advanced Materials* 24 (2012) 5374-5378.
- [5] M. Tahir, N.S. Amin, *Applied Catalysis B: Environmental* 142 (2013) 512-522.
- [6] S. Somasundaram, C.R.N. Chenthamarakshan, N.R. De tacconi, K. Rajeshwar, *International Journal of Hydrogen Energy* 32 (2007) 4661-4669.
- [7] P.D. Tran, S.K. Batabyal, S.S. Pramana, J. Barber, L.H. Wong, S.C. Loo, *Nanoscale* 4 (2012) 3875-3878.
- [8] S.X. Ouyang, H. Tong, N. Umezawa, J.Y. Cao, P. Li, Y.P. Bi, Y.J. Zhang, J.H. Ye,

- Journal of the American Chemical Society 134 (2012) 1974-1977.
- [9] S. Hara, H. Irie, *Applied Catalysis B: Environmental* 115-116 (2012) 330– 335.
- [10] H. Lv, L. Ma, P. Zeng, D. Ke, T. Peng, *Journal of Materials Chemistry* 20 (2010) 3665-3672.
- [11] B. Girginer, G. Galli, E. Chiellini, N. Bicak, *International Journal of Hydrogen Energy* 34 (2009) 1176-1184.
- [12] Q.J. Xiang, B. Cheng, J.G. Yu, *Applied Catalysis B: Environmental* 138-139 (2013) 299-303.
- [13] S.W. Cao, J. Fang, M.M. Shahjamali, F.Y.C. Boey, J. Barber, S.C.J. Loo, C. Xue, *RSC Advances* 2 (2012) 5513-5515.
- [14] F. Quarto, C. Sunseri, S. Piazza, M. Romano, *Journal of Physical Chemistry B* 101 (1997) 2519-2525.
- [15] Z.M. Li, P.Y. Zhang, T. Shao, X.Y. Li, *Applied Catalysis B: Environmental* 125 (2012) 350-357.
- [16] W.K. Chang, K.K. Rao, H.C. Kuo, J.F. Cai, M.S. Wong, *Applied Catalysis A: General* 321 (2007) 1-6.
- [17] Z.Y. Wang, B.B. Huang, Y. Dai, X.Y. Qin, X.Y. Zhang, P. Wang, H.X. Liu, J.X. Yu, *Journal of Physical Chemistry C* 113 (2009) 4612–4617.
- [18] J. Lv, T. Kako, Z.S. Li, Z.G. Zou, J.H. Ye, *Journal of Physical Chemistry C* 114 (2010) 6157–6162.
- [19] X.C. Wang, K. Maeda, A. Thomas, K. Takanabe, G. Xin, J.M. Carlsson, K. Domen, M. Antonietti, *Nature Materials* 8 (2009) 76-80.



- [20] K. Maeda, X.C. Wang, Y. Nishihara, D. Lu, M. Antonietti, K. Domen, *Journal of Physical Chemistry C* 113 (2009) 4940–4947.
- [21] G.G. Zhang, J.S. Zhang, M.W. Zhang, X.C. Wang, *Journal of Materials Chemistry* 22 (2012) 8083-8091.
- [22] X.B. Chen, S.H. Shen, L.J. Guo, S.S. Mao, *Chemical Reviews* 110 (2010) 6503–6570.
- [23] D. Sarkar, C.K. Ghosh, S. Mukherjee, K.K. Chattopadhyay, *ACS Applied Materials & Interfaces* 5 (2013) 331-337.
- [24] H.W. Bai, J. Juay, Z.Y. Liu, X.X. Song, S.S. Lee, D.D. Sun, *Applied Catalysis B: Environmental* 125 (2012) 367-374.
- [25] L.L. Xu, J.G. Guan, W.D. Shi, L.J. Liu, *Journal of Colloid and Interface Science* 377 (2012) 160–168.
- [26] M. Moriya, T. Minegishi, H. Kumagai, M. Katayama, J. Kubota, K. Domen, *Journal of the American Chemical Society* 135 (2013) 3733-3735.
- [27] Y.P. Yuan, S.W. Cao, Y.S. Liao, L.S. Yin, C. Xue, *Applied Catalysis B: Environmental* 140-141 (2013) 164-168.
- [28] Y.C. Chen, Y.C. Pu, Y.J. Hsu, *Journal of Physical Chemistry C* 116 (2012) 2967-2975.
- [29] J.B. Mu, B. Chen, M.Y. Zhang, Z.C. Guo, P. Zhang, Z.Y. Zhang, Y.Y. Sun, C.L. Shao, Y.C. Liu, *ACS Applied Materials & Interfaces* 4 (2012) 424-430.
- [30] J. Zhang, J.G. Yu, Y.M. Zhang, Q. Li, J.R. Gong, *Nano Letters* 11 (2011) 4774-4779.

- [31] F.K. Meng, Z.L. Hong, J. Arndt, M. Li, M.J. Zhi, F. Yang, N.Q. Wu, *Nano Research* 5 (2012) 213-221.
- [32] S.C. Yan, S.B. Lv, Z.S. Li, Z.G. Zou, *Dalton Transactions* 39 (2010) 1488-1491.
- [33] S.C. Yan, Z.S. Li, Z.G. Zou, *Langmuir* 25 (2009) 10397-10401.
- [34] J.L. Wu, F.C. Chen, Y.S. Hsiao, F.C. Chien, P.L. Chen, C.H. Kuo, M.H. Huang, C.S. Hsu, *ACS Nano* 5 (2011) 959-967.
- [35] B. Wu, T.Z. Oo, X.L. Li, X.F. Liu, X.Y. Wu, E.K.L. Yeow, H.J. Fan, N. Mathews, T.C. Sum, *Journal of Physical Chemistry C* 116 (2012) 14820-14825.
- [36] S.W. Cao, Y.P. Yuan, J. Fang, M.M. Shahjamali, F.Y.C. Boey, J. Barber, S.C.J. Loo, C. Xue, *International Journal of Hydrogen Energy*, 38 (2013) 1258-1266.
- [37] Y. Wang, X. Wang, M. Antonietti, *Angewandte Chemie International Edition* 51 (2012) 68-89.
- [38] A. Vinu, *Advanced Functional Materials* 18 (2008) 816-827.
- [39] A. Thomas, A. Fischer, F. Goettmann, M. Antonietti, J.-O Müller, R. Schlögl, J.M. Carlsson, *Journal Materials Chemistry* 18 (2008) 4893-4908.
- [40] Q. Xiang, J. Yu, M. Jaroniec, *Journal of Physical Chemistry C* 115 (2011) 7355-7363.
- [41] J.B. Mu, C.L. Shao, Z.C. Guo, M.Y. Zhang, Z.Y. Zhang, P. Zhang, B. Chen, Y.C. Liu, *Journal of Materials Chemistry* 22 (2012) 1786-1793.
- [42] Y. Na, M. Wang, J.X. Pan, P. Zhang, B. Åkerman, L.C. Sun, *Inorganic Chemistry* 47 (2008) 2805-2810.
- [43] S. Caramori, V. Cristino, R. Argazzi, L. Meda, C.A. Bignozzi, *Inorganic*

Chemistry 49 (2010) 3320-3328.

[44] F. Wang, W.G. Wang, X.J. Wang, H.Y. Wang, C.H. Tung, L.Z. Wu, *Angewandte Chemie International Edition* 50 (2011) 3193-3197.

[45] H.F. Cheng, B.B. Huang, Y.Y. Liu, Z.Y. Wang, X.Y. Qin, X.Y. Zhang, Y. Dai, *Chemical Communications* 48 (2012) 9729-9731.

[46] X. Y. Chen, Y. Zhou, Q. Liu, Z.D. Li, J.G. Liu, Z.G. Zou, *ACS Applied Materials & Interfaces* 4 (2012) 3372-3377.

[47] H. Xu, S.X. Ouyang, P. Li, T. Kako, J.H. Ye, *ACS Applied Materials & Interfaces* 5 (2013) 1348-1354.

[48] V.I. Klimov, D.W. McBranch, C.A. Leatherdale, M.G. Bawendi, *Physical Review B* 60 (1999) 13740-13749.

## Figure captions

**Fig. 1** XRD patterns of g-C<sub>3</sub>N<sub>4</sub>, In<sub>2</sub>O<sub>3</sub>, and 10 wt% In<sub>2</sub>O<sub>3</sub>-g-C<sub>3</sub>N<sub>4</sub>.

**Fig. 2** TEM image of (a) g-C<sub>3</sub>N<sub>4</sub>; (b) In<sub>2</sub>O<sub>3</sub>; and (c) 10 wt% In<sub>2</sub>O<sub>3</sub>-g-C<sub>3</sub>N<sub>4</sub>; (d) HRTEM image of 10 wt% In<sub>2</sub>O<sub>3</sub>-g-C<sub>3</sub>N<sub>4</sub>. Inset of Fig. 2a is the SEM image of g-C<sub>3</sub>N<sub>4</sub>.

**Fig. 3** UV-vis absorption spectra of g-C<sub>3</sub>N<sub>4</sub>, In<sub>2</sub>O<sub>3</sub>, and 10 wt% In<sub>2</sub>O<sub>3</sub>-g-C<sub>3</sub>N<sub>4</sub>.

**Fig. 4** XPS spectra of 10 wt% In<sub>2</sub>O<sub>3</sub>-g-C<sub>3</sub>N<sub>4</sub>: (a) C 1s; (b) N 1s; (c) In 3d; (d) O 1s.

**Fig. 5** (a) Plots of photocatalytic H<sub>2</sub> evolution amount versus irradiation ( $\lambda > 420$  nm) time for different samples (5mg); (b) Comparison of H<sub>2</sub> evolution amount over different samples (5 mg) after visible light irradiation for 4 hours.

**Fig. 6** (a) TEM image of 20 wt% In<sub>2</sub>O<sub>3</sub>-g-C<sub>3</sub>N<sub>4</sub>; (b) Cycling test of photocatalytic H<sub>2</sub> evolution for 10 wt% In<sub>2</sub>O<sub>3</sub>-g-C<sub>3</sub>N<sub>4</sub>.

**Fig. 7** Comparison of CH<sub>4</sub> production amount from photocatalytic CO<sub>2</sub> reduction after 4-h UV-vis irradiation (a) over different samples (20 mg) without any cocatalyst; (b) over 10 wt% In<sub>2</sub>O<sub>3</sub>-g-C<sub>3</sub>N<sub>4</sub> (20 mg) with and without Pt loading.

**Fig. 8** Transient photocurrent responses for the g-C<sub>3</sub>N<sub>4</sub>, In<sub>2</sub>O<sub>3</sub>, and 10 wt% In<sub>2</sub>O<sub>3</sub>-g-C<sub>3</sub>N<sub>4</sub> samples.

**Fig. 9** (a) Steady-state PL spectra and (b) Time-resolved transient PL decay for pure g-C<sub>3</sub>N<sub>4</sub> and the 10 wt% In<sub>2</sub>O<sub>3</sub>-g-C<sub>3</sub>N<sub>4</sub>.

**Fig. 10** Schematic illustration of the photocatalytic process for H<sub>2</sub> evolution and CO<sub>2</sub> reduction on the In<sub>2</sub>O<sub>3</sub>-g-C<sub>3</sub>N<sub>4</sub> nanohybrids.

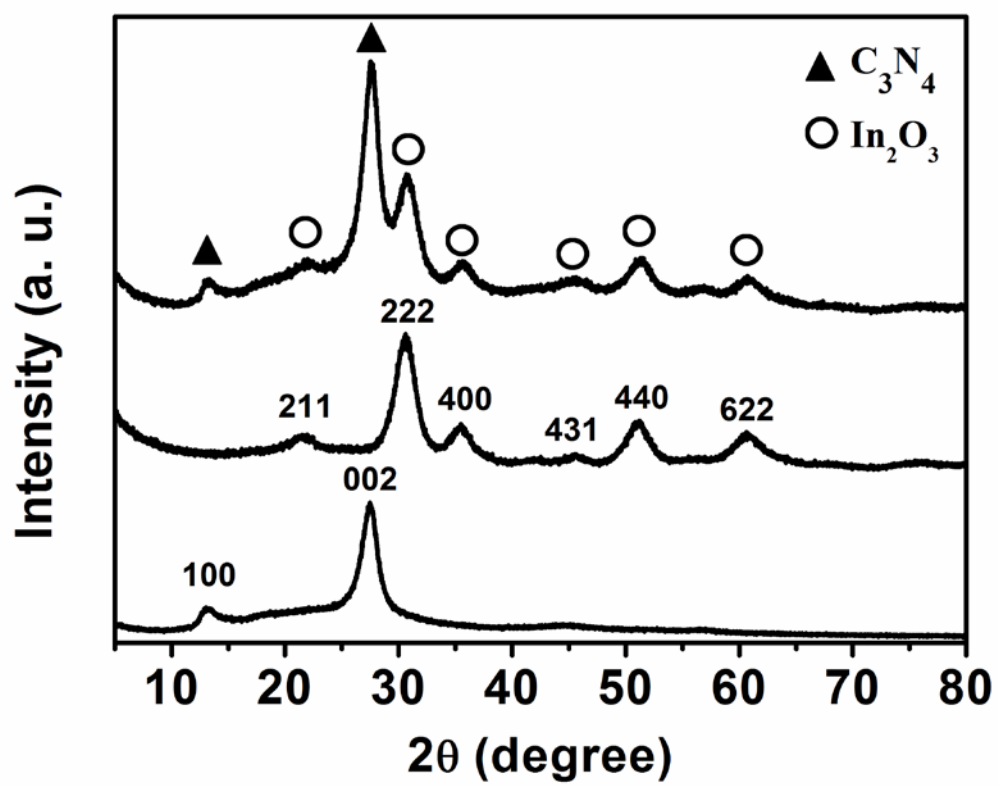
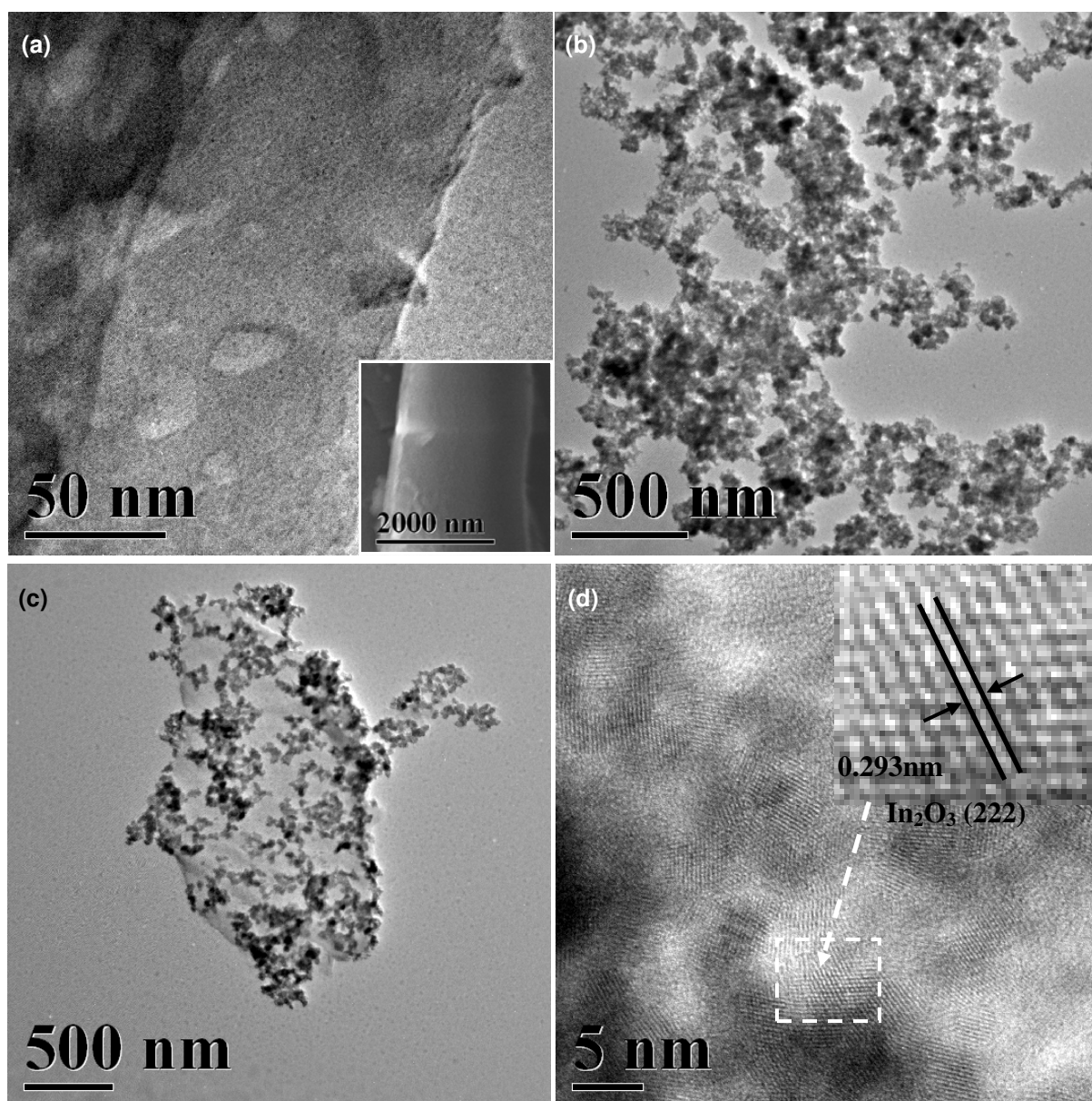


Fig. 1



**Fig. 2**

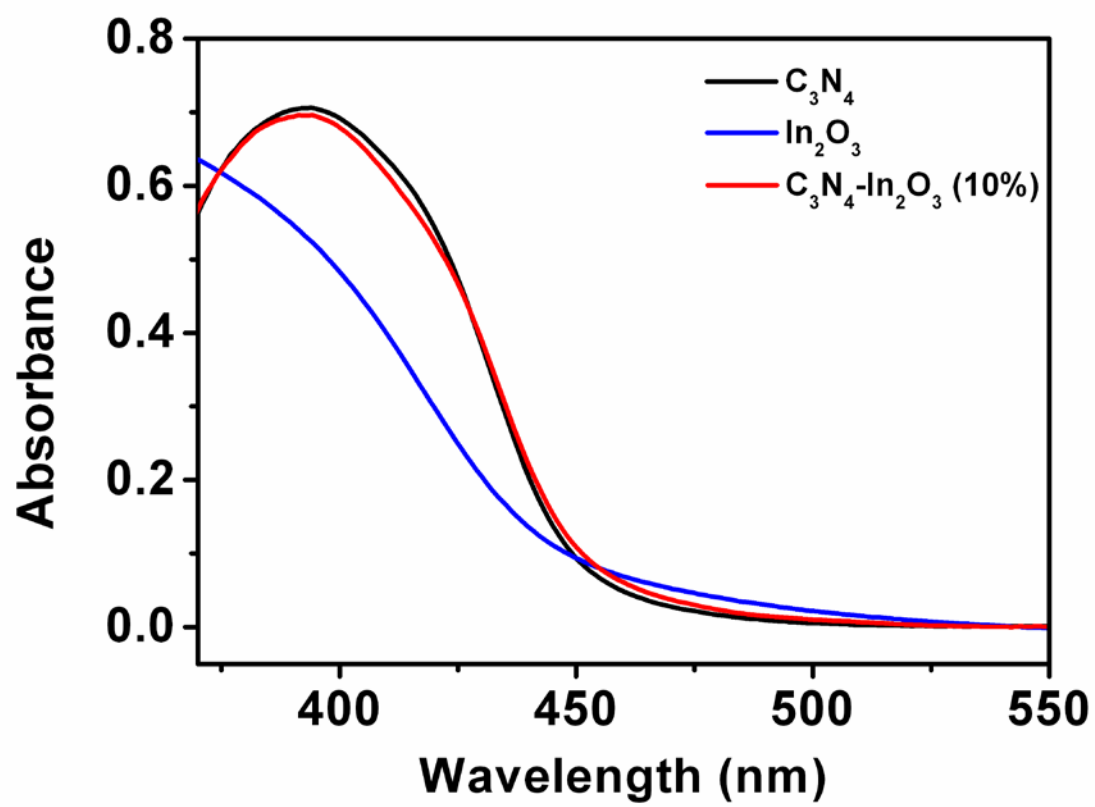


Fig. 3

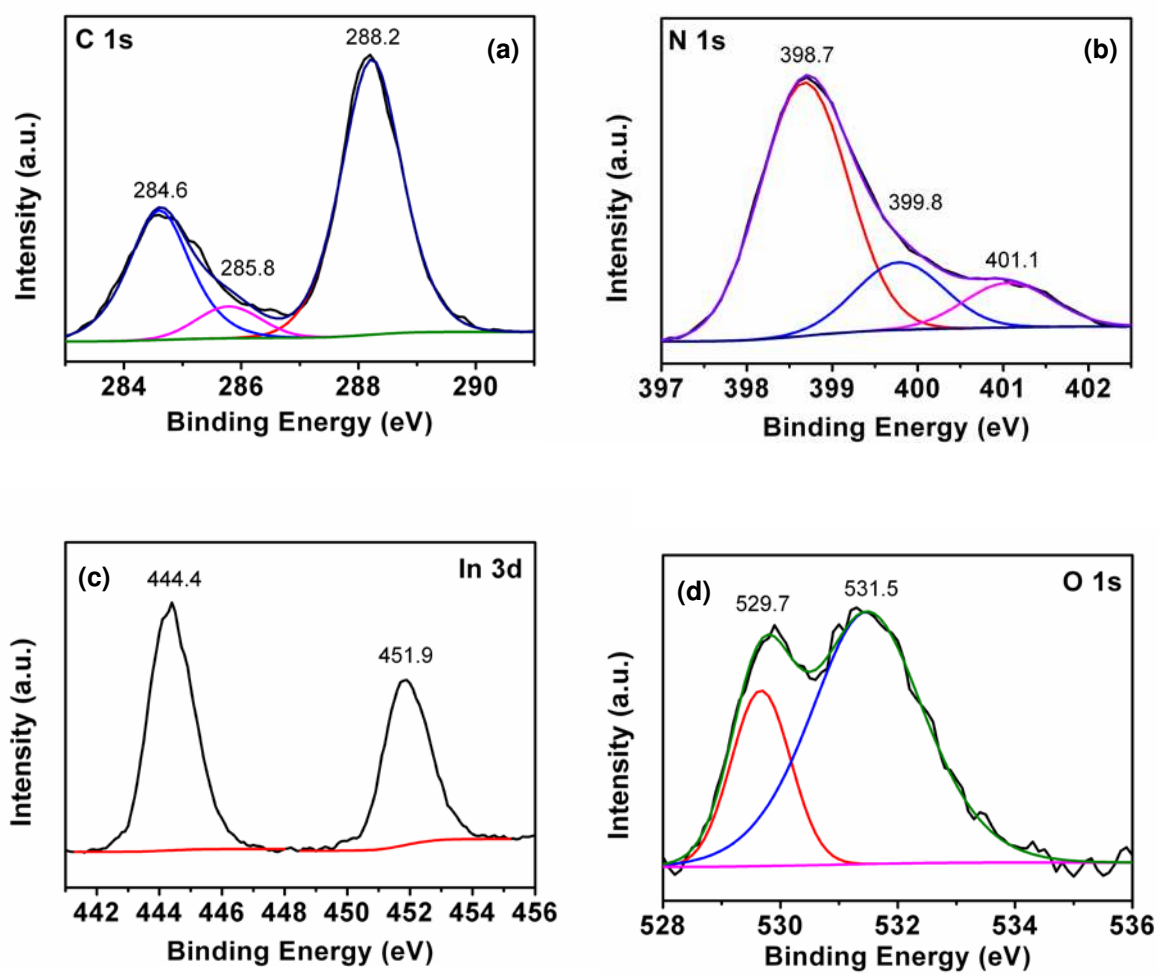
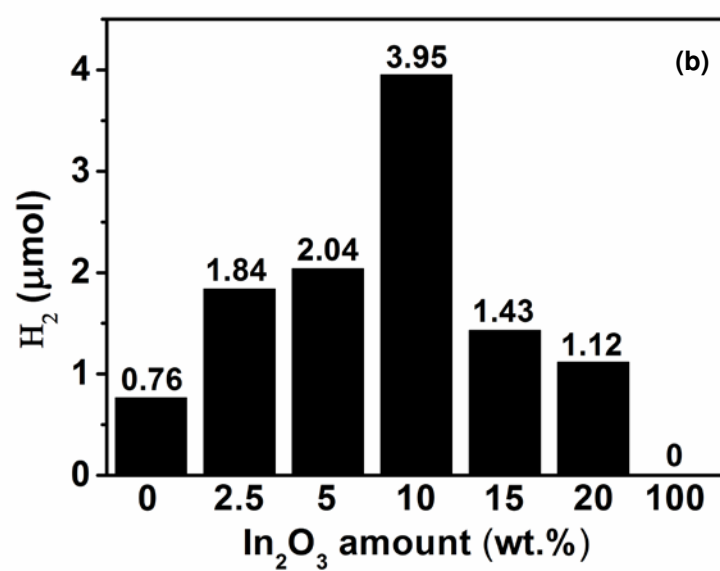
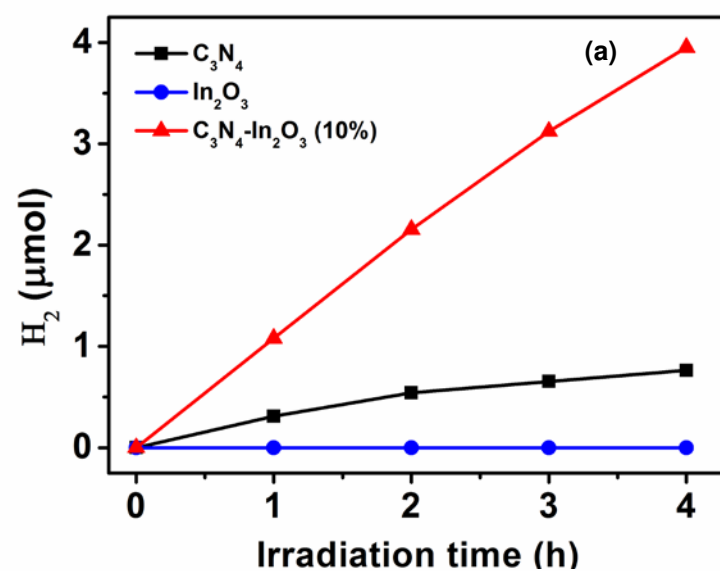
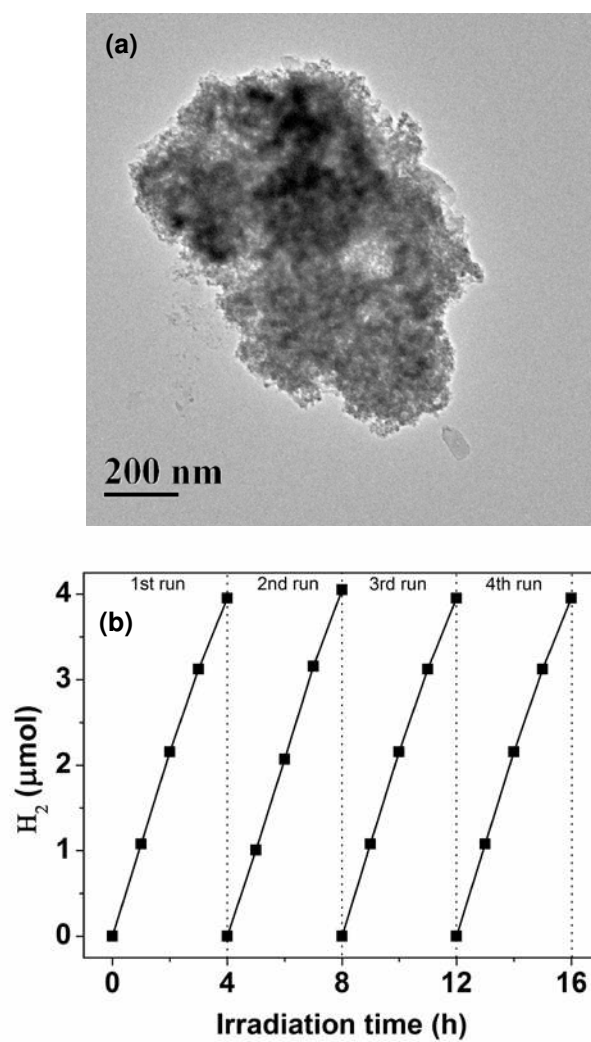


Fig. 4





**Fig. 5**



**Fig. 6**

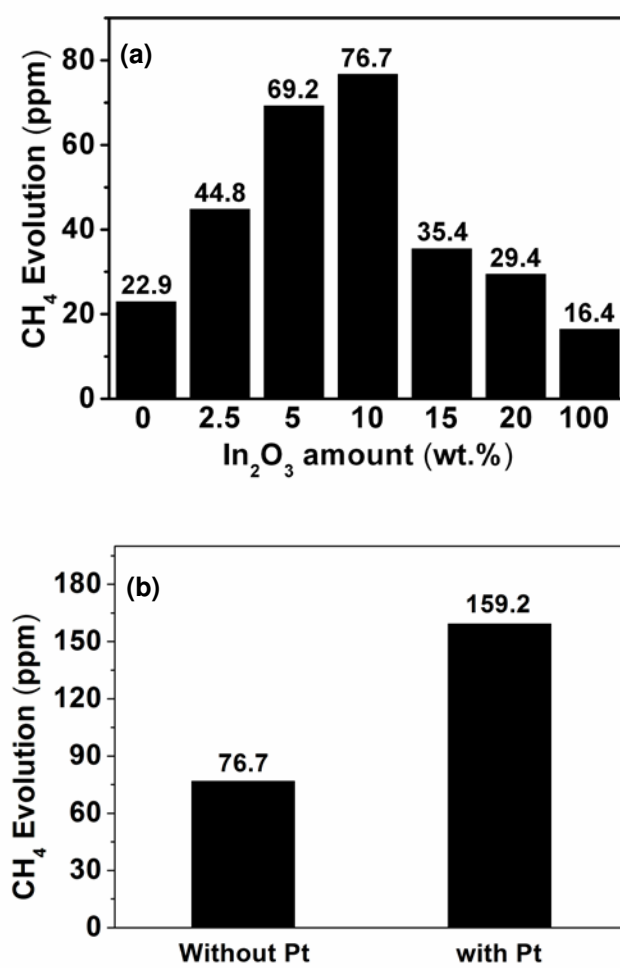


Fig. 7

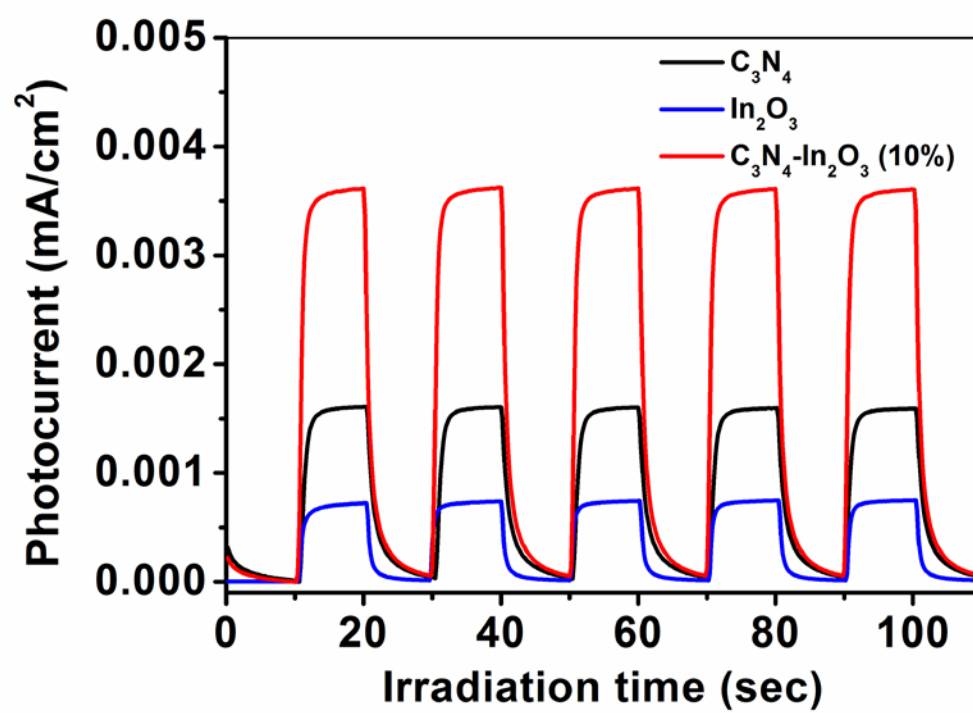


Fig. 8

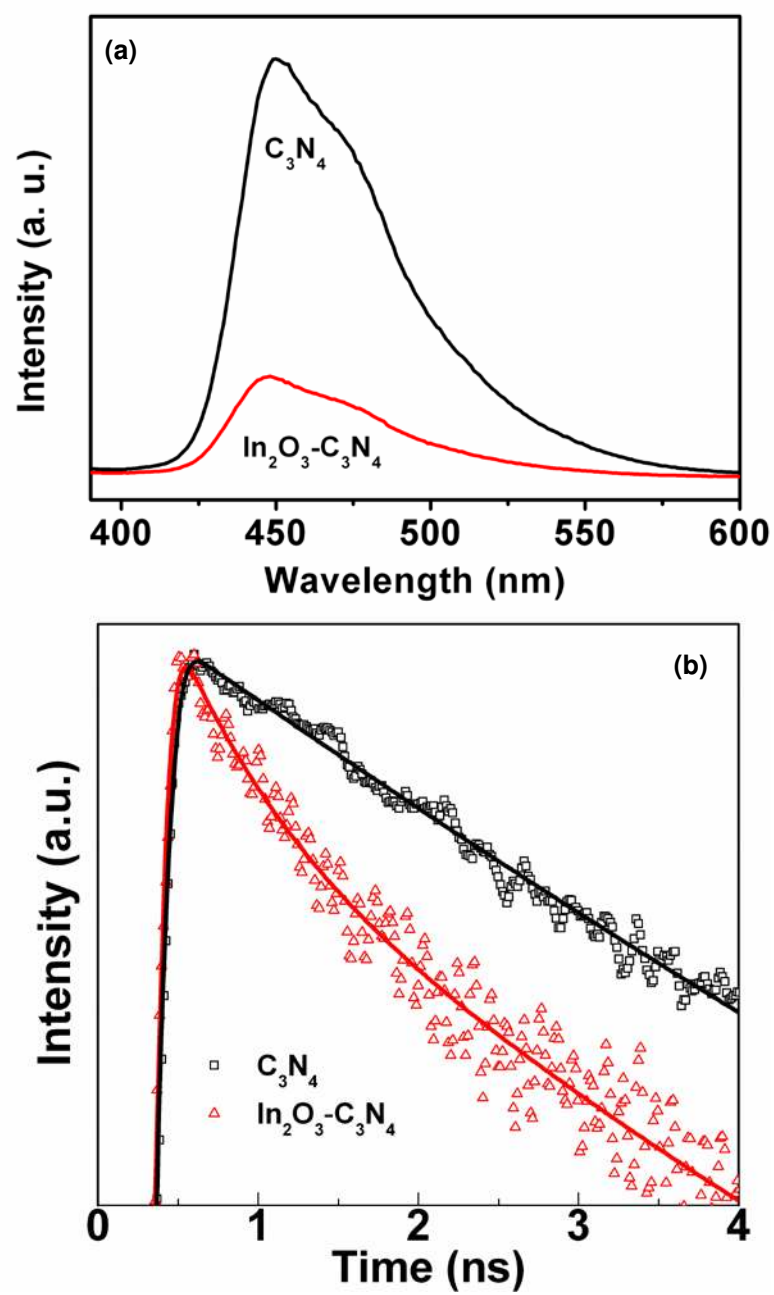


Fig. 9

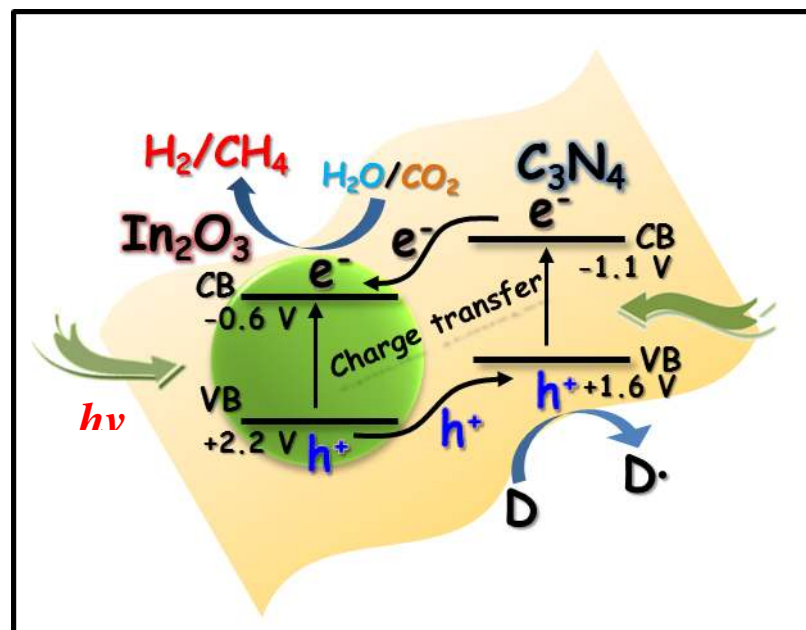


Fig. 10